npj | systems biology and applications

Article

Published in partnership with the Systems Biology Institute

https://doi.org/10.1038/s41540-025-00601-2

MMP9 shapes cell mechanics to enable collective invasion in cancer

Asadullah[1,3], Sarbajeet Dutta[1,3], Sumon Kumar Saha[1,3], Anisha Karmakar[2,3], Nikita Sharma[1], Sudikshaa Vijayakumar[1] & Shamik Sen[1,2] ✉

Cooperation among phenotypically distinct sub-populations within a tumor plays a key role in cancer progression. In this study, we investigated how proteolytic heterogeneity supports collective cancer invasion. In invasive MDA-MB-231 breast cancer cells which exhibit considerable variability in MMP9 expression, we show that MMP9 knockdown cells are notably smaller and softer than control cells. A computational model revealed that the invasiveness of mixed clusters containing both proteolytic and non-proteolytic cells depends on cell-cell adhesion, with non-proteolytic cell invasion requiring close proximity to proteolytic neighbors. When we assigned non-proteolytic cells the same size and stiffness as proteolytic ones, the overall invasiveness declined–highlighting that small size and deformability of non-proteolytic cells are essential for sustained collective invasion. We validated these predictions experimentally using spheroid invasion assays showing that mixed spheroids of control and MMP9 knockdown cells are the most invasive. Together, our findings demonstrate that interplay between MMP9 expression and biophysical properties enables collective invasion through enrichment of and matrix degradation by high MMP9 expressing cells at the invasive front, and squeezing of low MMP9 expressing cells through the remodeled matrix.

Intratumor heterogeneity in phenotypic and genotypic factors, such as gene expression, cell biophysical properties, and metastatic potential, have all been linked to cancer progression. Changes in cellular properties due to genetic, microenvironmental factors and other reversible changes lead to intra-tumor phenotypic and functional heterogeneity[1]. The coexistence of heterogeneous sub-populations within the same tumor raises the possibility of cooperation between them[2]. Such cooperation, as documented between poorly invasive melanoma and proteolytically active melanoma cells[3], may be beneficial for tumor growth, treatment resistance and collective invasion[4].

Two important biophysical characteristics of cells that have been demonstrated to influence cancer invasion and metastasis include cell size and cell/nuclear deformability[5–7]. Research has indicated that softer and smaller cells, such as cancer stem cells (CSCs), can have an advantage in invasion through the tumor stroma[8,9]. Interestingly, studies have also shown that cellular populations with more heterogeneity have a greater tendency to form secondary tumors, indicating that phenotypic heterogeneity may be a major mediator of metastasis[10]. However, the degree of heterogeneity in cell deformability and size within these heterogeneous cell clusters, and their relative contributions to collective cancer invasion, remain incompletely understood.

The invasion of cancer cells into the surrounding stromal tissue is the first stage of metastasis. For epithelial malignancies, this invasion necessitates breaching of the basement membrane (BM). After breaching the BM, cells move through a dense network of stromal extracellular matrix (ECM), which is mainly made up of fibrillar collagen I[11]. A successful cancer invasion is often associated with the ability of the cell to remodel the BM and stromal ECM components. This is achieved by matrix metalloproteinases (MMPs), a group of enzymes that can mediate ECM remodeling by degrading the major ECM components[12]. Degradation of collagen is a sequential process; though collagen degradation is initiated by collagenases such as MMP14[13], once degradation is initiated, collagen fibrils are further cleaved by gelatinases into smaller peptides[14]. While soluble MMPs such as MMP2 and MMP9 are classified as gelatinases, they are capable of degrading non-fibrillar collagen[15,16]. Moreover, MMP9 has also been shown to degrade native collagen fibrils[17]. Interestingly, matrix stiffening—a hallmark of several epithelial cancers[18], has been shown to drive increased activity of soluble MMP9 in invasive cancer cell lines[19]. Notably, metastatic MDA-MB-231 and HT-1080 cell lines exhibit a 100-fold higher expression of MMP9 compared to non-invasive cells, with no change in MMP2 expression[20]. Upon activation by MMP14, soluble MMPs secreted at sites of invadopodia, diffuse into the surrounding

[1]Department of Biosciences and Bioengineering, IIT Bombay, Mumbai, India. [2]Koita Center for Digital Health, IIT Bombay, Mumbai, India. [3]These authors contributed equally: Asadullah, Sarbajeet Dutta, Sumon Kumar Saha, Anisha Karmakar. ✉e-mail: shamiks@iitb.ac.in

matrix and degrade the matrix thereby creating paths permissive of migration[21].

Interestingly, using a zebrafish-melanoma xenograft model, Hurlstone and co-workers showed that intrinsically invasive cells possessing protease activity co-invade with sub-populations of less invasive cells, a phenomenon referred to as 'cooperative invasion'[3]. Inhibition of proteolytic activity has been shown to induce cell rounding and cell/nuclear softening, with nuclear softening sustaining protease-independent cell migration[22]. Therefore, 'cooperative invasion' may be enabled by MMP-dependent tuning of cell biophysical properties leading to enrichment of more invasive cells, i.e., high MMP expressing cells, at the invasive front. In this study, we address this possibility using a combination of experiments and computational modeling. We first document heterogeneity in MMP9 expression in MDA-MB-231 breast cancer cells, with MMP9 expression modulating cell size and cytoskeletal organization. Using a computational model of a heterogeneous cell cluster comprised of proteolytic cells mimicking MMP9-expressing cells and non-proteolytic cells mimicking MMP9 knockdown cells, we then show that cell-cell adhesion dictates the relative invasiveness of proteolytic and non-proteolytic cells, with non-proteolytic cells undergoing extensive deformation. Dramatic drop in population-level invasiveness was observed when size and deformability of non-proteolytic cells were set to that of proteolytic cells. Spheroid invasion experiments revealed highest invasiveness of spheroids containing control and knockdown cells. Collectively, our findings suggest MMP9-dependent tuning of cell biophysical properties is critical for sustaining invasiveness of a proteolytically heterogeneous population.

Results

MMP9 expression dictates cell biophysical properties

To study the importance of proteolytic heterogeneity in cancer invasion, heterogeneity in MMP9 expression was assessed in less migratory MCF-7 cells and highly invasive MDA-MB-231 breast cancer cells[23] using FACS. Consistent with the differences in baseline motility of the two cell lines, compared to MCF-7 cells where only 42% of the population was MMP9 positive, 99% of MDA-MB-231 cells were MMP9 positive (Supplementary Fig. 1). However, considerable heterogeneity in MMP9 expression was observed in MDA-MB-231 cells (hereafter referred to as MDA cells) (Fig. 1A). Biophysical profiling of MMP9 high and MMP9 low expressing cells FACS sorted from MDA cells revealed increased spreading and invasiveness in MMP9 high cells (Supplementary Fig. 2, Supplementary Movie 1). EMT profiling of these sub-populations revealed increased vimentin expression in MMP9 high cells (Supplementary Fig. 2D). E-cadherin levels remained unaltered between MMP9 high and MMP9 low cells.

To directly probe the extent to which MMP9 expression and/or its activity modulates cell biophysical properties, control and MMP9 knockdown stable cell lines were generated using lentiviral transduction (referred to as CTL and KD cells, respectively). In addition, KD cells were stably transfected with catalytically inactive MMP9 mutant (E402A) construct to generate ΔCat (referred to as DC) cells, which are incapable of matrix remodeling (Fig. 1B). While westerns of total cell lysates from KD cells revealed substantial reduction in MMP9 expression at the population level, FACS profiling revealed low MMP9 expression in 20% of the population (Fig. 1C, Supplementary Fig. 3). While MMP9 expression was restored in DC cells, there was considerable heterogeneity in MMP9 expression at the single cell level (Supplementary Fig. 3). However, in gelatin zymography experiments, MMP9 activity was substantially lower in both KD and DC cells (Fig. 1C). Interestingly, cell proliferation was reduced in both KD and DC cells (Supplementary Fig. 4A). Further, vimentin expression was reduced in both KD and DC cells (Supplementary Fig. 4B). When seeded on top of 3D collagen gels, in comparison to CTL and DC cells which exhibited well spread morphologies, KD cells were more rounded (Fig. 1D, E). Further, cell stiffness measurements using AFM revealed substantial cortical softening in KD cells compared to CTL cells (Fig. 1F, G). In comparison, cortical stiffness of DC cells was comparable to that of CTL cells. Collectively, these results suggest that cell size and deformability are dictated by MMP9 expression.

Biophysical heterogeneity between proteolytic and non-proteolytic cells dictates population-level invasiveness

Heterogeneity in MMP9 expression combined with prominent cell rounding and softening observed upon MMP9 knockdown suggests that variation in MMP9 expression is intimately tied to heterogeneity in cell biophysical properties, specifically size and deformability. To assess the combinatorial influence of functional and biophysical heterogeneity on cancer invasion, we made use of our previously established Cellular Potts Model (CPM)-based formalism[24] using which we recently demonstrated the importance of biophysical heterogeneity in enhancing cancer invasiveness[9]. In this model, we track scattering of a cell cluster positioned at the center of a rectangular grid (at time $t = 0$) surrounded by randomly positioned ECM fibers of varying lengths (Fig. 2A). For this study, the cell cluster comprised of a mix of proteolytic (green) and non-proteolytic cells (red), with their relative proportions varying from 0% to 100%. Simulations were performed with a combination of proteolytic and non-proteolytic cells positioned randomly in the cluster to avoid any positional bias (Fig. 2B, Supplementary Fig. 5A). The size of the proteolytic cells (A_p) and non-proteolytic cells (A_{kd}) were taken as the average size of CTL cells and KD cells determined experimentally, i.e., $A_p = 856\ \mu m^2$, $A_{np} = 400\ \mu m^2$ (Fig. 1E). Cell scattering is enabled by matrix degradation mediated by MMP9 secreted by proteolytic cells thereby generating paths for migration. MMP9 secretion, diffusion and degradation were modeled using reaction diffusion kinetics integrated into the CPM formalism (see Computational Method section for details).

Our simulation framework consists of 'cell' pixels, 'matrix' (i.e., ECM) pixels and 'fluid' pixels. Spatiotemporal evolution of the system achieved by random movement of neighboring 'cell' pixels of two different cells, or between neighboring 'cell' and 'fluid' pixels, is based on the total system energy (Equation 1, Computational Method section). 'Matrix' pixels do not participate in this update, but are degraded by MMPs as outlined above; upon degradation, 'matrix' pixels are converted to 'fluid' pixels. The total system energy has four components; the first component is dependent on the adhesion energies between cell-cell (J_{cc}), cell-matrix ($J_{cm} = 16k_BT/L$) and cell-fluid ($J_{cf} = 32k_BT/L$) pixels, with J_{cc} varied to mimic collective cell migration ($J_{cc} = 1k_BT/L$), single cell migration ($J_{cc} = 40k_BT/L$) and intermediate cell-cell adhesion ($J_{cc} = 16k_BT/L$). The second and third terms in the energy equation correspond to energetic penalties associated with deviations of cell size/perimeter from their preferred values, and depend on bulk stiffness (λ_a) and line tension (λ_p) of the cells. To mimic experimental observations, proteolytic cells were assigned λ_a/λ_p values twice as that of non-proteolytic cells, i.e., $\lambda_a{}^{p} = 1\,E/L^4$, $\lambda_a{}^{np} = 0.5\,E/L^4$, $\lambda_p{}^{p} = 0.5\,E/L^2$ and $\lambda_p{}^{np} = 0.25\,E/L^2$. The last term corresponds to the intrinsic motility of cells, with proteolytic cells being more motile than non-proteolytic cells, as observed experimentally[19].

Simulations performed for varying proportion of proteolytic cells and varying cell-cell adhesion (J_{cc}) were analyzed to determine both individual and population-level invasiveness (Fig. 2C). For all values of J_{cc}, increase in the percentage of proteolytic cells (p) led to increased scattering. Though quantification of individual cell translocation (D), i.e., end-to-end displacement, revealed statistically significant increase with p, there was considerable heterogeneity within each sub-population (Fig. 2D, Supplementary Fig. 5B). The population-averaged net displacement ($\bar{D}$) was insensitive to J_{cc}, and exhibited a sigmoidal dependence on the proportion of proteolytic cells with a saturating trend beyond 55% proteolytic fraction (Supplementary Fig. 5C). To probe the relative contributions of proteolytic and non-proteolytic cells to population-level invasiveness, translocation of the two sub-populations were quantified. While proteolytic and non-proteolytic cells exhibited comparable migration at $J_{cc} = 1$, proteolytic cells migrated more than non-proteolytic cells for $J_{cc} = \{16, 40\}$ (Fig. 2E, Supplementary Fig. 5D).

To study the extent to which differences in cell stiffness observed between CTL and KD cells influenced population-level invasiveness, simulations were performed by keeping the properties of the proteolytic

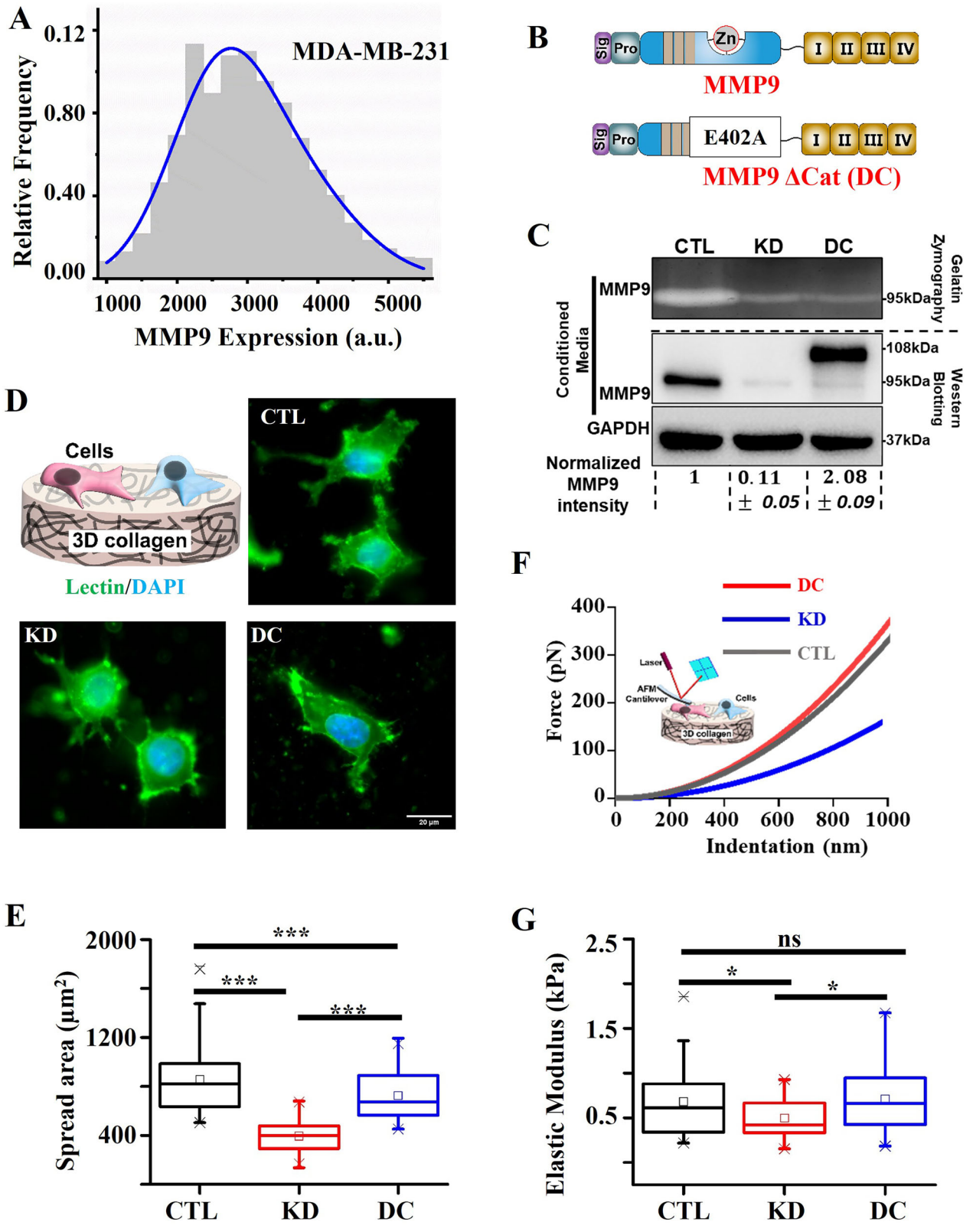

cells fixed and varying λ^{np}/λ^{p}, i.e., the ratio of deformability (area and perimeter constraints) of non-proteolytic cells to that of proteolytic cells. Softening the non-proteolytic cells relative to proteolytic cells led to increased population-level invasiveness at J_{cc} = {16, 40} (Fig. 2F, Supplementary Fig. 6A). In line with this, when $\bar{D}$ was fit using the equation $\bar{D} = \bar{D}_{p0} + (\bar{D}_{p100} - \bar{D}_{p0})\frac{p^n}{(p^n+K^n)}$ ($\bar{D}_{p0}$ and $\bar{D}_{p100}$ represent the values of $\bar{D}$ corresponding to p = 0% and p = 100%, respectively), the half-saturation value (K) was found to reduce with softening of non-proteolytic cells, with the cooperativity index (n) exhibiting no particular trend (Supplementary Fig. 6B).

Next, to probe the importance of spatial positioning of proteolytic and non-proteolytic cells on population-level invasiveness, we performed

Fig. 1 | Effect of MMP9 perturbations on cell spreading and cell stiffness of MDA-MB-231 breast cancer cells. A Representative MMP9 expression in MDA-MB-231 breast cancer cells assessed using FACS. **B** Establishment of MDA-MB-231 cells stably transfected with non-targeting sequence (CTL), MMP9 knockdown sequence (KD), and shKD cells expressing catalytically inactive MMP9 ΔCat(DC): Schematic representation of structure of full length MMP9 and catalytically inactive MMP9ΔCat (DC). **C** Gelatin zymography and western blotting using cell secreted conditioned media (CM) of CTL, KD, and DC cells. Equal volume of cell lysates were loaded and GAPDH used as loading control. **D** Representative Lectin/DAPI stained images of CTL, KD, and DC cells seeded on top of 3D collagen gels. **E** Quantification of cell spreading of CTL, KD and DC cells on Col gels ($n \geq 106$ cells per condition across $N = 3$ independent experiments). Scale Bar = 10 μm. Stars denote statistical significance: *** p value < 0.001. One-way ANOVA with Tukey's test was used for comparing means. **F** Representative force-indentation curves obtained by indenting CTL, KD, and DC cells with a pyramidal AFM probe were fitted with Hertz model to estimate cortical stiffness. **G** Quantification of cell cortical stiffness of CTL, KD, and DC cells on Col gels ($n \geq 37$ cells per condition across $N = 3$ independent experiments). Stars denote statistical significance: * p value <0.05, ns: not significant. One-way ANOVA with Tukey's test was used for comparing means.

simulations by spatially arranging the proteolytic and non-proteolytic cells into inner and outer core as depicted in Supplementary Fig. 7A. For these set of simulations, the population-averaged net displacement of the proteolytic cells when placed in the outer core were significantly higher compared to the non-proteolytic cells (Supplementary Fig. 7B).

While insightful, all the above simulations were performed with varying proportions of proteolytic and non-proteolytic cells. To more closely mimic the heterogeneity in MMP9 expression observed in MDA-MB-231 cells, simulations were performed for $J_{cc} = 40$ of a population consisting of three sub-populations (Lo, Med and Hi) with varying MMP secretion rates (λ_{MMP}) (Supplementary Fig. 5E). The relative proportion of the three sub-populations were based on the average (μ_{MMP9}) and the standard deviation (σ_{MMP9}) in MMP9 expression determined from FACS data (Fig. 1A). While Lo sub-population correspond to cells possessing MMP9 expression less than ($\mu_{MMP9} - \sigma_{MMP9}$), Hi sub-population correspond to cells with MMP9 expression greater than ($\mu_{MMP9} + \sigma_{MMP9}$). The intermediate MMP9 expressing cells were categorized as MMP9 Med cells. Based on this characterization, the population comprised on 11% Lo, 70% Med and 19% Hi cells (Supplementary Fig. 5E). MMP9 Lo and MMP9 Hi cells were assumed to have size and deformability same as that of non-proteolytic and proteolytic cells, respectively. Properties of MMP Med cells was chosen as average of the proteolytic and non-proteolytic cells. Invasiveness of the heterogeneous population was compared with homogenous populations of non-proteolytic, Lo, Med and Hi cells, respectively. Among the homogeneous populations, invasiveness increased with increase in MMP secretion rate with MMP Hi cells being most invasiveness (Supplementary Fig. 5F). Remarkably, invasiveness of the heterogeneous population which consisted of 70% Med cells was more than the MMP9 Hi population. For $J_{cc} = 1$ and $J_{cc} = 16$, invasiveness of heterogeneous population was comparable to the homogeneous Hi population, but more than the homogeneous Lo and Med populations. Taken together, these results suggest that biophysical heterogeneity, the proportion of proteolytic cells, and the spatial positioning of proteolytic and non-proteolytic cells collectively regulate population-level invasiveness.

Deformability, initial position and proteolytic neighbors dictate invasiveness of non-proteolytic cells

Though increase in the fraction of proteolytic cells (i.e., p) led to increase in population-level invasiveness, considerable heterogeneity in displacements of both proteolytic and non-proteolytic cells was observed for each simulation condition. To uncover the factors underlying such large variation in invasiveness of individual cells, the contributions of cell shape (quantified by cell circularity, C), initial spatial position within the cell cluster (R_i) and the number of proteolytic neighbors (N_p) to individual cell invasiveness, we performed t-distributed stochastic neighbor embedding (t-SNE) analysis. For all values of J_{cc}, increase in p led to increase in the proportion of cells exhibiting increased invasiveness (Fig. 3A, B, Supplementary Fig. 8). Non-proteolytic cells that were more invasive were positioned at the outer periphery of the cell cluster and/or had higher number of neighboring proteolytic cells. Importantly, for all values of J_{cc}, lower circularity of non-proteolytic cells in comparison to control cells suggests that non-proteolytic cells underwent greater deformation, with the difference being most prominent at $J_{cc} = 1$ (Fig. 3C). Plotting cell circularity as a function of cell displacement revealed greater deformation of non-proteolytic cells for lower proteolytic cell fraction, particularly for the cells exhibiting low displacement (Fig. 3D, Supplementary Fig. 9A). These cells undergoing large deformations were placed somewhat towards the periphery of the cell cluster, i.e., $(60 \leq R_i \leq 80)\mu$m (Fig. 3E, Supplementary Fig. 9B).

To probe for possible coordination in movement between proteolytic and non-proteolytic cells, proteolytic and non-proteolytic cells within individual cell clusters were numbered (Fig. 4A) and the spatiotemporal evolution of pairs of 'closely spaced' proteolytic and non-proteolytic cells (i and j respectively) tracked by measuring the intercellular distance (d_{ij}) and the cosine of the angle between their directions of motion ($cos\theta$) (Fig. 4B). Given the sizes of proteolytic and non-proteolytic cells, the distance between the cell centroids of a pair of cells in their undeformed state was approximated to be 28 μm by assuming each cell as a circle and estimating their radius. Since non-proteolytic cells undergo extensive deformation during the simulations, these cells were assumed to closely follow neighboring proteolytic cells if $d_{ij} \leq (1.5 \times 28 \approx 45)\mu$m over a period of 600 MCS (i.e., a third of the total simulation duration) and $cos\theta \approx 1$. Indeed, for each condition (i.e., $p = \{29, 57, 71\}$%), pairs of cells were identified (e.g., $J_{cc} = 1$: cell pairs (30, 38), (40, 41) and (62, 64) respectively; $J_{cc} = 16$: cell pairs (49, 66), (23, 24) and (14, 22) respectively; $J_{cc} = 40$: cell-pairs (38, 47), (10, 11) and (2, 7) respectively) which were closely located throughout the duration of the simulations and moved in the same direction indicative of coordinated movement, with the non-proteolytic cells exhibiting more deformation (i.e., lower circularity) compared to the proteolytic cells for greater fraction of time (Fig. 4C, Supplementary Fig. 10A). In contrast, for several cell pairs that were initially closely spaced (e.g., $J_{cc} = 1$: cell pairs (8, 14), (7, 33) and (12, 20) respectively; $J_{cc} = 16$: cell pairs (52, 61), (44, 67) and (1, 7) respectively; $J_{cc} = 40$: cell-pairs (18, 47), (35, 44) and (23, 24) respectively), gradual increase in intercellular distance with time was observed with no directional coordination (Supplementary Fig. 10B). In addition to highlighting increased deformation of non-proteolytic cells, these results suggest that a fraction of non-proteolytic cells follow paths created by neighboring proteolytic cells.

Small size and softness of non-proteolytic cells sustain collective invasion

Thus far, our simulations were performed by assuming non-proteolytic cells to be smaller and softer than compared to proteolytic cells, i.e., we assumed non-proteolytic cells to have properties similiar to that of MMP9 knockdown cells (i.e., KD cells). However, in contrast to KD cells, DC cells–which express catalytically inactive MMP9 are also non-proteolytic, but comparable in size and deformability to those of control cells. To assess the impact of differences in biophysical properties between proteolytic and non-proteolytic cells on population-level invasiveness, simulations were performed by varying the size/deformability of non-proteolytic cells (red, pink and blue combinations) compared to the earlier simulations (black points) that mimic our experimental observations (Fig. 5A). For the first set (red points), both proteolytic and non-proteolytic cells were assumed to have same deformability (i.e., ${\lambda_a}^p = {\lambda_a}^{np} = 1\,E/L^4, {\lambda_p}^p = {\lambda_p}^{np} = 0.5\,E/L^2$), but their cell sizes were different (i.e., $A_p = 856\ \mu m^2$, $A_{np} = 400\ \mu m^2$). For the second set (pink points), both proteolytic and non-proteolytic cells were assumed to have same size (i.e., $A_p = A_{np} = 856\ \mu m^2$), but their deformabilities were distinct (i.e., ${\lambda_a}^p = 1\,E/L^4, {\lambda_a}^{np} = 0.5\,E/L^4, {\lambda_p}^p = 0.5\,E/L^2$ and ${\lambda_p}^{np} = 0.25\,E/L^2$). For the third set (blue points), both proteolytic and

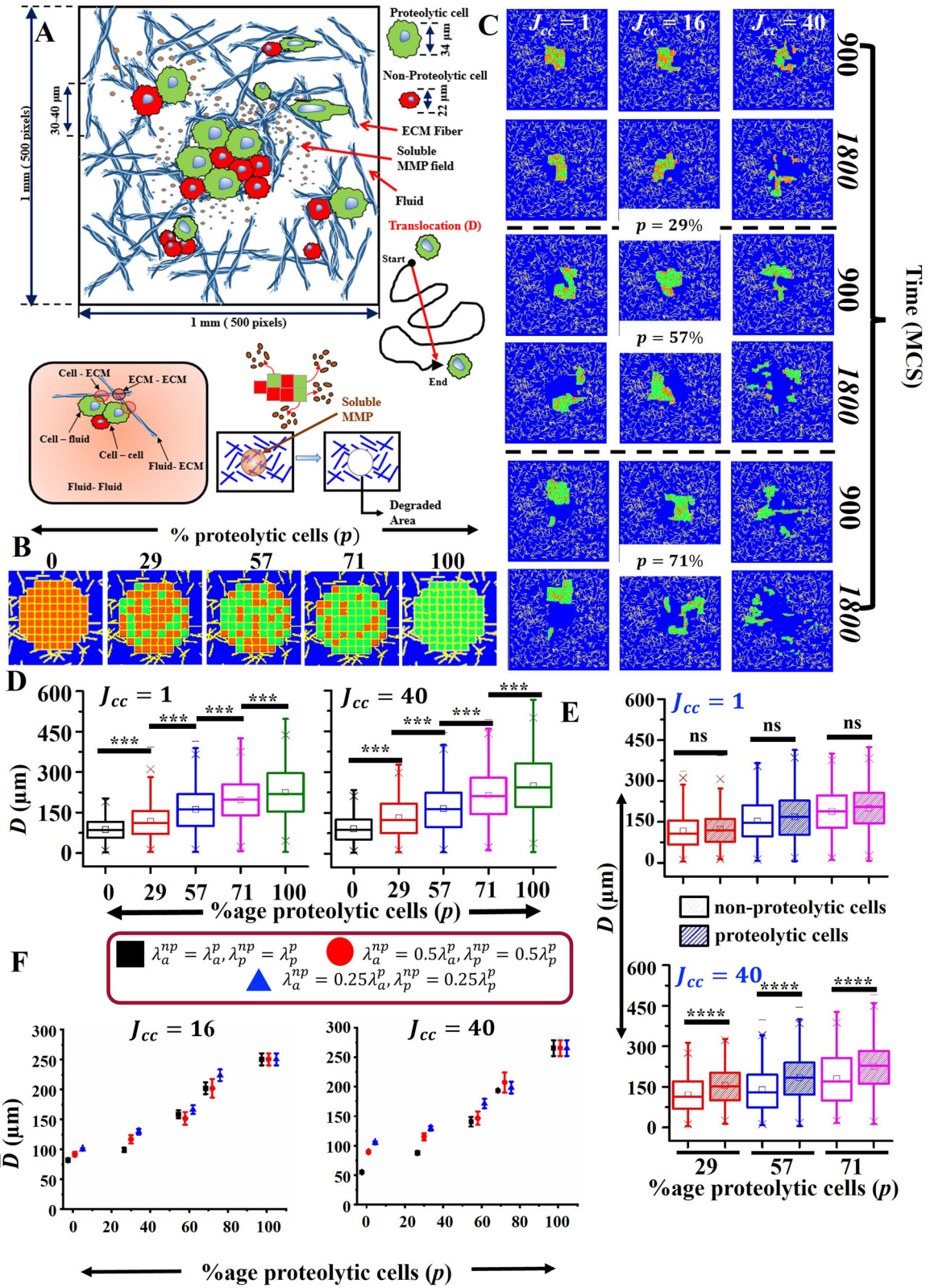

non-proteolytic cells were assumed to be of same size and deformability, i.e., $A_p = A_{np} = 856\ \mu m^2$ and $\lambda_a{}^p = \lambda_a{}^{np} = 1\,E/L^4$. For ease of reference, the four simulation conditions are referred to as HCHD (i.e., heterogeneity in cell size and deformability, or, proteolytic and non-proteolytic cells differ in both cell size and deformability), HCSD (i.e., heterogeneity in cell size only, or, proteolytic and non-proteolytic cells differ in cell size only, but possess same deformability), SCHD (i.e., heterogeneity in deformability only, or, proteolytic and non-proteolytic cells differ in deformability only, but are of same size), and SCSD (i.e., proteolytic and non-proteolytic cells possess same cell size and deformability).

In comparison to HCHD condition, population-level invasiveness dropped for all the three conditions (i.e., HCSD, SCHD and SCSD

Fig. 2 | Computational model of cancer invasion by a phenotypically and functionally heterogeneous cell cluster. A Schematic of model. Cancer invasion was simulated by studying scattering of a cell cluster consisting of a combination of proteolytic (green) and non-proteolytic (red) cells. At the start of simulations, the cell cluster is positioned at the center of a 1 × 1 mm^2 2D space mimicking the extracellular matrix (ECM). The ECM comprises of randomly positioned ECM fibers (blue helical lines); the white space corresponds to the interstitial fluid. ECM degradation is mediated by MMP9 molecules secreted by proteolytic cells, which diffuse into the surrounding ECM and degrade ECM fibers. Upon degradation, ECM gets converted to interstitial fluid. **B** Representative images of cell clusters showing the spatial distribution of proteolytic and non-proteolytic cells for varying %age of proteolytic cells (p). **C** Pattern of cell scattering at the end of 1800 MCS for varying p and varying extent of cell-cell adhesion (J_{cc}). **D** Quantification of end-to-end displacement (D) at varying p and $J_{cc} = \{16, 40\}$($n = 690$ cells per condition pooled from $N = 10$ independent simulations). Stars denote statistical significance: *** p value < 0.001. One-way ANOVA with Tukey's post hoc test was used for comparing means. **E** Quantification of displacements of proteolytic and non-proteolytic cells at varying p and $J_{cc} = \{16, 40\}$($N = 3$). Stars denote statistical significance: ns: non-significant, *p value < 0.05, *** p value < 0.001. One-way ANOVA with Tukey's post-hoc test was used for comparing means. **F** Comparison of population-averaged displacement ($\bar{D}$) as a function of p and $J_{cc} = \{16, 40\}$ for two different combinations of properties (λ_a, λ_p) of proteolytic and non-proteolytic cells. Black squares: ${\lambda_a}^{np} = 0.5{\lambda_a}^{p} = 0.5\,E/L^4$, ${\lambda_p}^{np} = 0.5{\lambda_p}^{p} = 0.25\,E/L^2$; Red circles: ${\lambda_a}^{np} = 0.5{\lambda_a}^{p} = 0.5\,E/L^4$, ${\lambda_p}^{np} = 0.5{\lambda_p}^{p} = 0.25\,E/L^2$; Blue triangles: ${\lambda_a}^{np} = 0.25{\lambda_a}^{p} = 0.25\,E/L^4$, ${\lambda_p}^{np} = 0.25{\lambda_p}^{p} = 0.125\,E/L^2$. Error bars represent ± SEM. Stars denote statistical significance: ns: non-significant, ** p value <0.01, *** p value <0.001, **** p value <0.0001. $t$test was used for comparing means.

conditions) for most combinations of J_{cc} and p, with maximum drop observed for SCSD condition at $J_{cc} = 40$ (Fig. 5B). Though proteolytic cells exhibited greater displacements compared to non-proteolytic cells for most of the conditions (Supplementary Fig. 11), when proteolytic and non-proteolytic cells were deformable to the same extent, i.e., HCSD and SCSD conditions, proteolytic cells underwent more deformation compared to non-proteolytic cells (Fig. 5C). Furthermore, quantification of the radial position of individual cells at the end of the simulations (R_{end}) from the initial center of the cell cluster (at $t = 0$) revealed significant drop in the extent of cell scattering of non-proteolytic cells for SCSD conditions (Fig. 5D). Collectively, these results suggest that biophysical heterogeneity between proteolytic and non-proteolytic cells is essential for sustaining invasiveness of a proteolytically heterogeneous cell cluster.

Heterospheroids comprised of control and knockdown cells are maximally invasive

To correlate our simulation predictions with experiments, spheroid invasion experiments were performed with homospheroids containing CTL, KD and DC cells alone, or heterospheroids formed by combining CTL cells with KD cells or with DC cells in 1:1 ratio. For ease of referencing, the homospheroids are referred to as CTL, KD and DC spheroids, respectively, and heterospheroids referred to as CTL-KD and CTL-DC spheroids, respectively (Fig. 6A). Considerable variation in sizes of homospheroids and heterospheroids were observed with no statistically significant difference (Fig. 6B).

For studying spheroid invasion, homospheroids and heterospheroids were implanted in 3D collagen gels on Day 0 and cell scattering was tracked over a period of 2 days (Fig. 6C, Supplementary Movies 2, 3). For tracking invasion of heterospheroids, the two cell-types were transfected with two different fluorophores (GFP and RFP). At Day 2, minimal cell death was observed in the spheroid cores of CTL, KD and DC spheroids (Supplementary Fig. 12A). It was not possible to probe cell death in heterospheroids as one of the cell-types was RFP-tagged. Cell proliferation rates both in the spheroid cores and outside the core regions were comparable in both homospheroids and heterospheroids (Supplementary Fig. 12B). In spite of no difference in cell death and cell proliferation, imaging of Day 2 spheroids revealed substantial differences in the extent of outward scattering of the spheroids, with highest scattering observed in CTL-KD spheroids and lowest in KD and DC spheroids (Fig. 6C).

To gain further insight into the observed differences in invasiveness of different spheroids, invasion was quantified by drawing circles circumscribing the spheroids at Day 0 (designated at Zone 0 or Z_0), and then drawing concentric circles of width 200 μm, designated as zones Z_1, Z_2 and Z_3, respectively (Fig. 6D). Outward scattering/invasion of cells from the spheroids was quantified by counting the number of cells in each zone at Day 1 and Day 2 for the different conditions. Normalized cell scattering was quantified by first determining the zone-wise distribution of cells for a given condition (i.e., $n_{Z_i}, i = \{1, 2, 3\}$, corresponding to the number of cells in zone Z_i), and dividing by the total number of cells scattered (i.e., $n_{Z_1} + n_{Z_2} + n_{Z_3}$) by the corresponding number observed for CTL spheroids on Day 1 (representative calculation shown in detail in Supplementary Fig. 13). Comparison of normalized cell scattering revealed lowest invasiveness for KD and DC spheroids (Fig. 6E). In comparison, fastest invasion was observed for CTL-KD spheroids, with nearly twice as many cells in Z_1 compared to that of CTL cells. Increase in both CTL and KD cells were detected in outer zones at Day 2. Invasion of CTL-DC spheroids was comparable to that of CTL spheroids. Closeup time-lapse images of CTL-KD and CTL-DC heterospheroid scattering revealed enrichment of proteolytic cells at the invasive front in case of CTL-KD spheroids (Supplementary Movies 2, 3). Collectively, these results suggest that enrichment of and matrix remodeling by CTL cells at the invasive front, and squeezing of KD cells through the surrounding remodeled matrix collectively contributes to the highest invasiveness of CTL-KD spheroids.

Discussion

How does phenotypic heterogeneity drive cancer invasion? In this study, we addressed this question by first establishing a close relationship between MMP9 expression and cell biophysical properties in mesenchymal MDA-MB-231 cells. We show that MMP9 expression regulates cell spreading and cytoskeletal organization independent of its activity. By recapitulating these experimental observations in simulations with varying cell-cell adhesion (i.e., J_{cc}), we show proteolytic cells migrate more than non-proteolytic cells at moderate and low cell-cell adhesion, with softening of non-proteolytic cells further increasing population-level invasiveness for $p < 60\%$. Population-level invasiveness was suppressed when non-proteolytic cells were either similar in size to proteolytic cells, or possessed similar deformability. Remarkably, spheroids formed by combining CTL cells with KD cells were maximally invasive. In contrast, both KD and DC spheroids exhibited minimal invasion. Based on these findings, we propose a model wherein inverse correlation between MMP9 expression and cell mechanics facilitates collective invasion of a proteolytically heterogeneous cell cluster through enrichment of and matrix degradation by high MMP9 cells at the invasive front and squeezing of low MMP9 cells through the remodeled matrix (Fig. 7).

MMPs represent a class of proteases associated with matrix remodeling[12]. Of these, MMP9 has been implicated with cancer metastasis[15]. MMP9 molecules, packaged in exosomes[25], and secreted via protrusive structures such as invadopodia[21], diffuse into the surrounding matrix and mediate matrix degradation thereby enabling mesenchymal or 'path generating' mode of invasion. Matrix stiffening implicated in multiple epithelial cancers is associated with increased MMP9 secretion[19], with inhibition in MMP activity leading to cell rounding and cell/nuclear softening [22]. While we observed similar cell rounding and softening in KD cells, cytoskeletal organization remained unaltered in DC cells, suggesting that MMP9 proteolytic activity is not essential for sustaining cell spreading and migration. Recently, in an independent study, we demonstrated the presence of two integrin β1 binding sites on MMP9, with one of the binding sites mediating co-trafficking of MMP9 and integrin β1 to the cell membrane, and the other stabilizing integrin β1 on the cell membrane[21]. Thus, loss of cytoskeletal organization in KD cells may be a consequence of loss of focal adhesions that are necessary for anchoring the cytoskeleton.

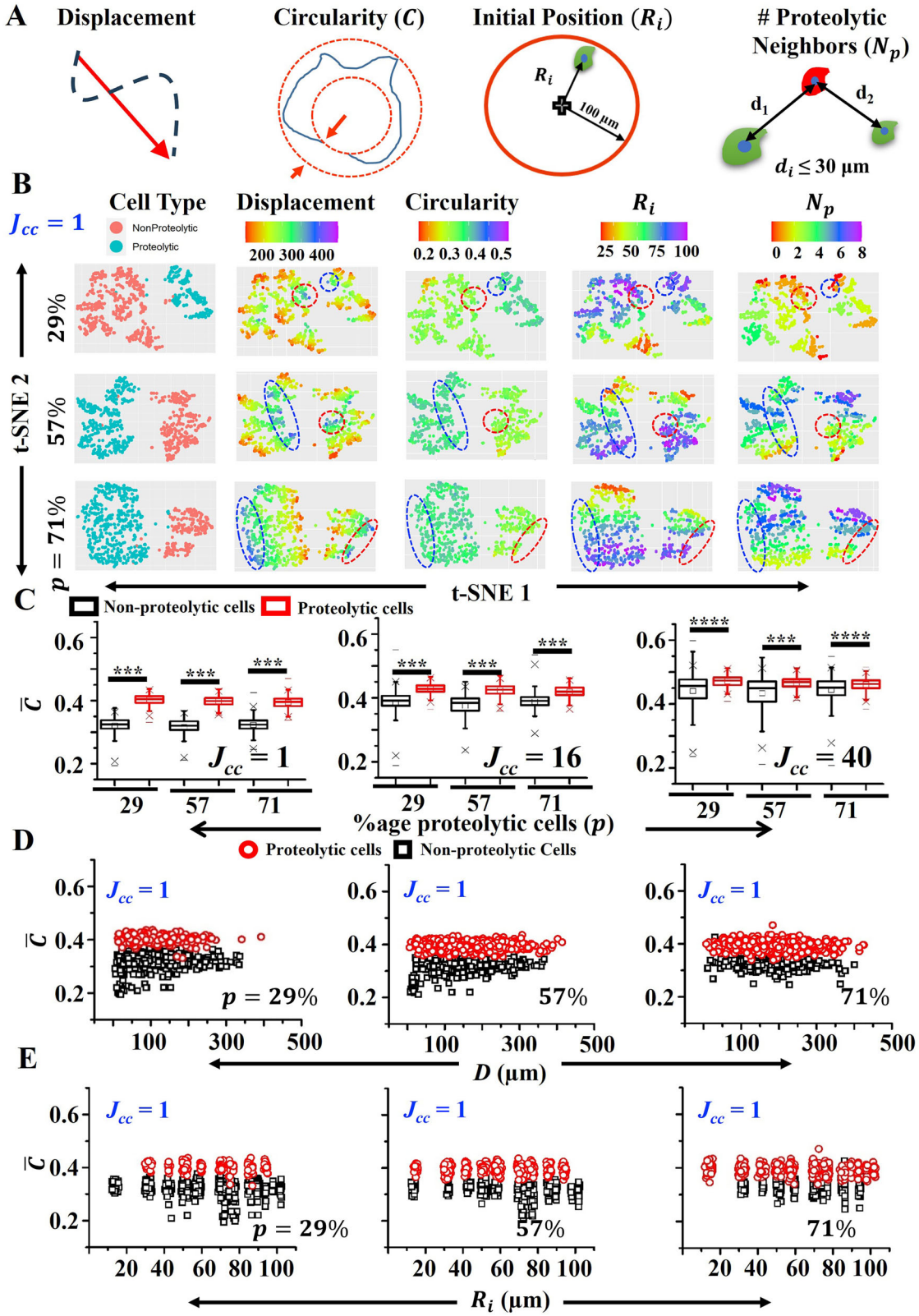

Fig. 3 | Parameters involved in co-operative collective migration. A Cell displacement (D), cell circularity (C), initial position (R_i), and the number of proteolytic neighbors (N_p) were used for t-SNE analysis. **B** tSNE-based 2D-embedding of simulation data corresponding to $J_{cc} = 1$ and varying proteolytic fraction (p) based on cell-type (i.e., non-proteolytic or proteolytic), D, C, R_i, and N_p. Red/blue dotted lines correspond to non-proteolytic/proteolytic cells exhibiting high D. **C** Box plot of time-averaged circularity ($\bar{C}$) of non-proteolytic and proteolytic cells for varying p across three adhesion energies ($n = 690$ cells per condition pooled from $N = 10$ independent simulations). Stars denote statistical significance: *** p value <0.001. One-way ANOVA with Tukey's post hoc test was used for comparing means. **D** Plot of $\bar{C}$ of non-proteolytic and proteolytic cells as a function of displacement for varying p and $J_{cc} = 1$ ($n = 690$ cells per condition pooled from $N = 10$ independent simulations). **E** Plot of $\bar{C}$ of non-proteolytic and proteolytic cells as a function of R_i for varying p and $J_{cc} = 1$ ($n = 690$ cells per condition pooled from $N = 10$ independent simulations).

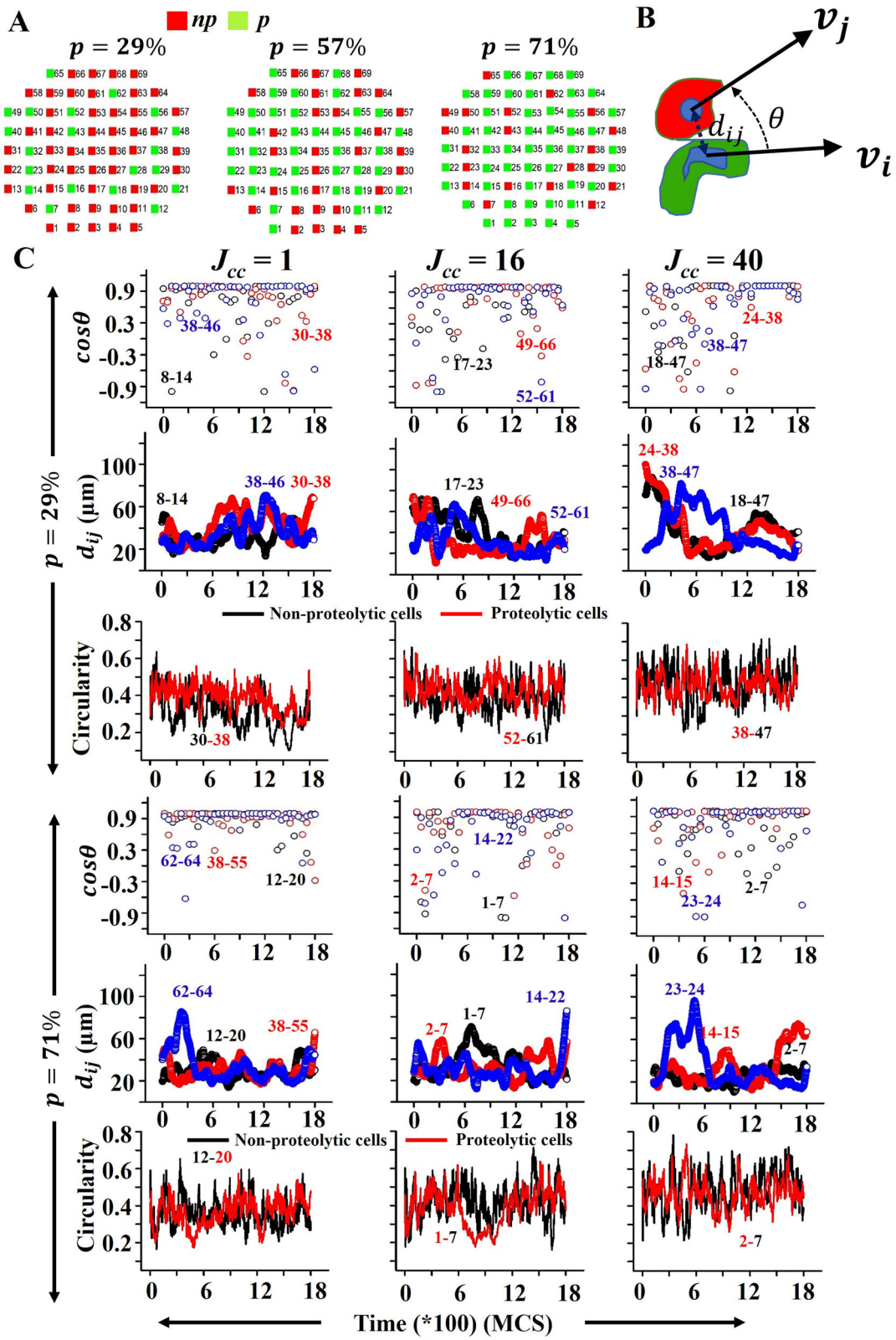

Fig. 4 | Spatiotemporal evolution of proteolytic and non-proteolytic cells during invasion. A Representation of positioning of proteolytic and non-proteolytic cells in spheroids of different compositions. **B** Vectorial representation of cos θ and intercellular distance ($d_{i,j}$) between a pair of proteolytic and non-proteolytic cells. **C** Time evolution of cos θ, d_{ij}, and circularity of pairs of proteolytic and non-proteolytic cells during invasion.

Epithelial to mesenchymal transition (EMT), associated with the activation of core transcription factors including Zeb, Twist, Snail and Slug, drives cancer progression through loss of cell-cell adhesions and gain of migration-associated traits. Though EMT was originally characterized as a binary process based on expression of the epithelial (E) marker E-cadherin and the mesenchymal (M) marker vimentin, a plethora of studies has established that EMT corresponds to a spectrum of states with varying levels of epithelial and mesenchymal markers[26–28].

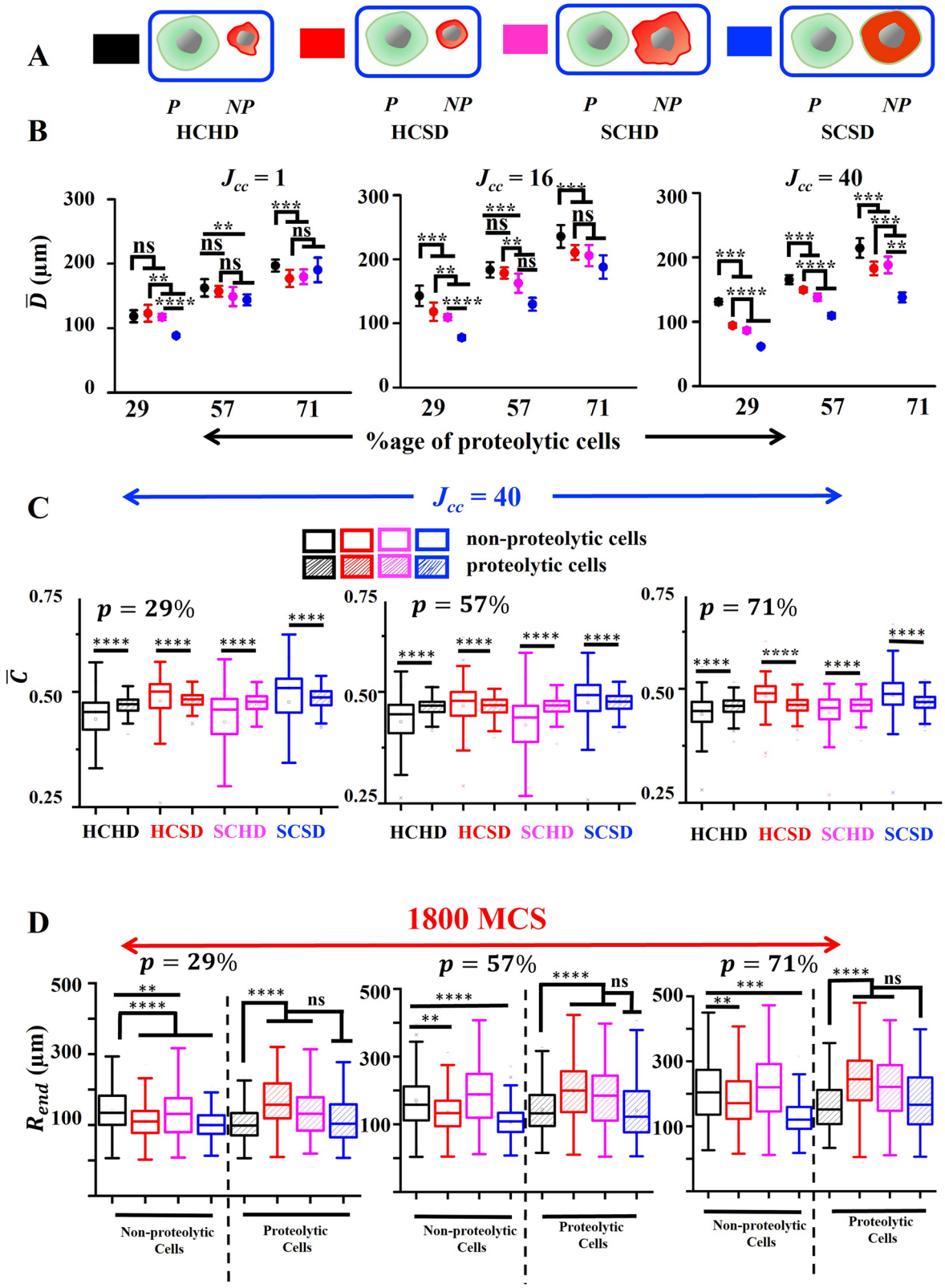

The intermediate states, also referred to as partial EMT (pEMT) or hybrid E/M states, have been associated with increased metastasis, poor survival and therapeutic resistance. By combining scRNAseq, bulk RNAseq and spatial transcriptomics data, a recent study demonstrated that while luminal breast cancers are homogeneous and possess epithelial traits, basal and TNBC tumors correspond to pEMT state with the presence of cells exhibiting mixed (i.e., E/M) gene signature and the coexistence of both epithelial and mesenchymal cell states[29]. Here, we document considerable heterogeneity in expression of the mesenchymal marker MMP9 in MDA-MB-231 cells. Such heterogeneity may arise spatially within the tumor depending on EMT inducing factors such as TGFβ secreted by stromal cells[30].

Fig. 5 | Invasiveness of proteolytically heterogeneous cell cluster for different combinations of cell size and deformability. A Simulations were performed for 4 conditions corresponding to varying combinations of cell size and deformability of proteolytic and non-proteolytic cells. These include heterogeneity in both cell size and deformability (HCHD, black points), heterogeneity in cell size but same deformability (HCSD, red points), heterogeneity in deformability but same cell size (SCHD, pink points), and same cell size and deformability (SCSD, blue points). **B** Quantification of average displacement ($\bar{D}$) for HCDC, HCSD, SCHD and SCSD conditions at varying p and $J_{cc} = \{1, 16, 40\}$ ($n = 690$ cells per condition pooled from $N = 10$ independent simulations). Stars denote statistical significance: ** p value <0.01, *** p value <0.001, **** p value <0.0001. One-way ANOVA with Tukey's post-hoc test was used for comparing means for each combination of p and J_{cc}. **C** Box plot of time-averaged circularity ($\bar{C}$) of non-proteolytic and proteolytic cells for HCDC, HCSD, SCHD, and SCSD conditions at varying p and $J_{cc} = 40$ ($n = 690$ cells per condition pooled from $N = 10$ independent simulations).. Stars denote statistical significance: ns: non-significant, **** p value <0.0001. One-way ANOVA with Tukey's post hoc test was used for comparing means. **D** Box-plot of radial scattering (R_{end}) of proteolytic and non-proteolytic cells for HCDC, HCSD, SCHD and SCSD conditions at varying p and $J_{cc} = 40$ ($n = 690$ cells per condition pooled from $N = 10$ independent simulations). Stars denote statistical significance: ns: non-significant, ** p value <0.01, *** p value <0.001, **** p value <0.0001. One-way ANOVA with Tukey's post-hoc test was used for comparing means.

Cell rounding and softening observed in KD cells, but not in DC cells, suggests that MMP9 expression influences cell biophysical properties. Tuning of MMP9 expression can thus give rise to cells of varying size and deformability, which is essential for cooperative invasion as demonstrated clearly in our simulations wherein differences in both cell size and cell deformability between proteolytic and non-proteolytic cells was important for population-level invasiveness. Despite no measurable difference in cell death and cell proliferation rates, CTL-KD spheroids were more invasive compared to CTL-DC spheroids. Increased invasiveness of CTL-KD spheroids was associated with increased scattering of CTL cells across all zones, with increase in zone-wise distribution from Day 1 to Day 2. Thus, the combination of simulations and experiments thus suggest that biophysical heterogeneity imparts more fluidity to the entire population resulting in increased invasiveness. Inability of KD spheroids to invade despite KD cells being softer highlights the importance of matrix degradation.

Due to fast proliferation of cancer cells, tumors grow under nutrient deprived and hypoxic conditions. In addition, matrix stiffening leads to collapse of blood vessels further limiting nutrient availability and increasing resistance to invasion. Invasion is an energy demanding process with higher ATP:ADP ratio in dense 3D collagen matrices reflective of increased energy requirement; in comparison, ATP:ADP ratio is less when cells migrate through aligned collagen matrices where steric hindrance is limited[31–33]. ATP generation is mediated by a combination of glycolysis and oxidative phosphorylation[34], with glycolysis essential for sustaining confined migration of MDA-MB-231 cells[35]. Since extracellular acidification in glycolysis is associated with MMP activation, cancer cells preferably invade in a proteolytic manner[36,37]. However, upon inhibition of MMP activity, cancer cells switch to an amoeboidal mode of migration[38,39]. Amoeboidal migration is sustained by cell and nuclear softening enabling cells to squeeze through pre-existing pores in the matrix[22]. Interestingly, recent studies have established amoeboidal mode of migration to be more energy-efficient that can be sustained by very low levels of oxidative phosphorylation[40,41]. Thus, MMP9 expression may be spatiotemporally modulated depending on oxygen and nutrient availability. Given the pros and cons of the two modes of migration, heterogeneity in MMP9 expression may enable cell clusters to invade optimally under varying conditions with MMP9 expression tuned dynamically depending on nutrient availability. Thus, highest invasiveness of CTL-KD spheroids may thus be partly attributed to reduction in overall energy requirement of the spheroids due to the presence of softer KD cells with very low energy demand.

The CPM framework has been successfully employed to recapitulate several aspects of cancer invasion observed experimentally[9,42,43]. Our experiments reveal a positive association between MMP9 expression and expression of the mesenchymal marker vimentin. In our simulations, we recapitulate different extents of EMT by varying J_{cc}, with $J_{cc} = 1$ corresponding to epithelial state, $J_{cc} = 40$ corresponding to mesenchymal state, and $J_{cc} = 16$ corresponding to pEMT state. Insensitivity of population-level invasiveness to cell-cell adhesion may be attributed to the lack of positional bias given to proteolytic cells and the extent of cell-cell rearrangements. This is evident at $J_{cc} = 1$ where both proteolytic and non-proteolytic cells exhibited comparable invasiveness; in comparison, with loss of cell-cell adhesion (i.e., at $J_{cc} = \{16, 40\}$), proteolytic cells exhibited greater displacements than non-proteolytic cells. Consistent with leader-follower behavior of cells documented experimentally[13], non-proteolytic cells exhibiting increased invasiveness were preferentially placed at the periphery of the cell cluster, and followed paths generated by neighboring proteolytic cells. Across all conditions, lower circularity of non-proteolytic cells irrespective of their initial position is indicative of their increased deformation mediated partly by stiffer proteolytic cells. Consequently, when non-proteolytic cells were set to be as large as or as stiff as proteolytic cells, the difference in circularities of the two cell types were reduced or lost leading to dramatic drop in population-level invasiveness.

In our simulations, when proteolytic cells were assumed to be twice as stiff as non-proteolytic cells as observed experimentally, population-level invasiveness exhibited a saturating trend for $p \approx 60\%$. When non-proteolytic cells were made softer (i.e., $\frac{1}{4}^{\text{th}}$ and $\frac{1}{8}^{\text{th}}$ as that of proteolytic cells), for $J_{cc} = \{16, 40\}$, population-level invasiveness for $p < 60\%$ increased, but remained unaltered at higher values of p. In contrast, for $J_{cc} = 1$, population-level invasiveness was insensitive to softening of non-proteolytic cells. These results suggest that cell-cell adhesion dictates the sensitivity of invasion efficiency to biophysical heterogeneity.

In conclusion, our study has unearthed a strong coupling between MMP9 expression and cell mechanics, and illustrates how this crosstalk between functional heterogeneity (i.e., MMP9 expression) and biophysical heterogeneity drives collective cancer invasion. Our simulations predict that optimal invasiveness is sustained by a threshold proportion of proteolytic cells which in turn depends on the extent of biophysical heterogeneity. However, in addition to differences in cell size and deformability, other factors such as the cell surface glycocalyx that modulates cell size[44] are also likely to influence collective invasion. The impact of microenvironmental factors such as nutrient/oxygen availability on spatiotemporal modulation of MMP9 expression and its impact on invasion needs to be ascertained. Future studies with cell lines exhibiting different extents of EMT will help to establish the generality of our findings, and also validate our predictions.

Methods

Experimental methods

Cell culture and generation of cell lines. MCF-7 and MDA-MB-231 cells were obtained from National Center for Cell Science (NCCS), Pune. Cells were cultured on 60 mm petri dishes (Tarsons, Cat # 960020) in media containing high glucose Dulbecco's Modified Eagle Medium (DMEM) (Gibco, Invitrogen, Cat # 12800-017) supplemented with 10% Fetal Bovine Serum (FBS, Gibco, Invitrogen, Cat # 10270106) and 1% antibiotic and antimycotic solution (HiMedia, Cat # A002). They were incubated at 37°C, in presence of 5% CO_2. At 80% confluency, cells were trypsinised by using 0.25% trypsin (HiMedia, Cat # TCL070) and passaged onto new dish. Cell proliferation and MMP9 heterogeneity were assessed in MCF-7 and MDA-MB-231 cells using fluorescence activated cell sorting (FACS) (BD FACS Aria Fusion). Cells at 60-70% confluence were trypsinized, fixed with 4% paraformaldehyde (PFA) and permeabilized with 97% ice-cold methanol. The pellets were resuspended in FACS buffer containing 1% FBS in phosphate-buffered saline (PBS). The samples were divided into tubes for unstained controls and stained samples. Staining was performed using Ki-67 (CST Cat # 9129, 1:400

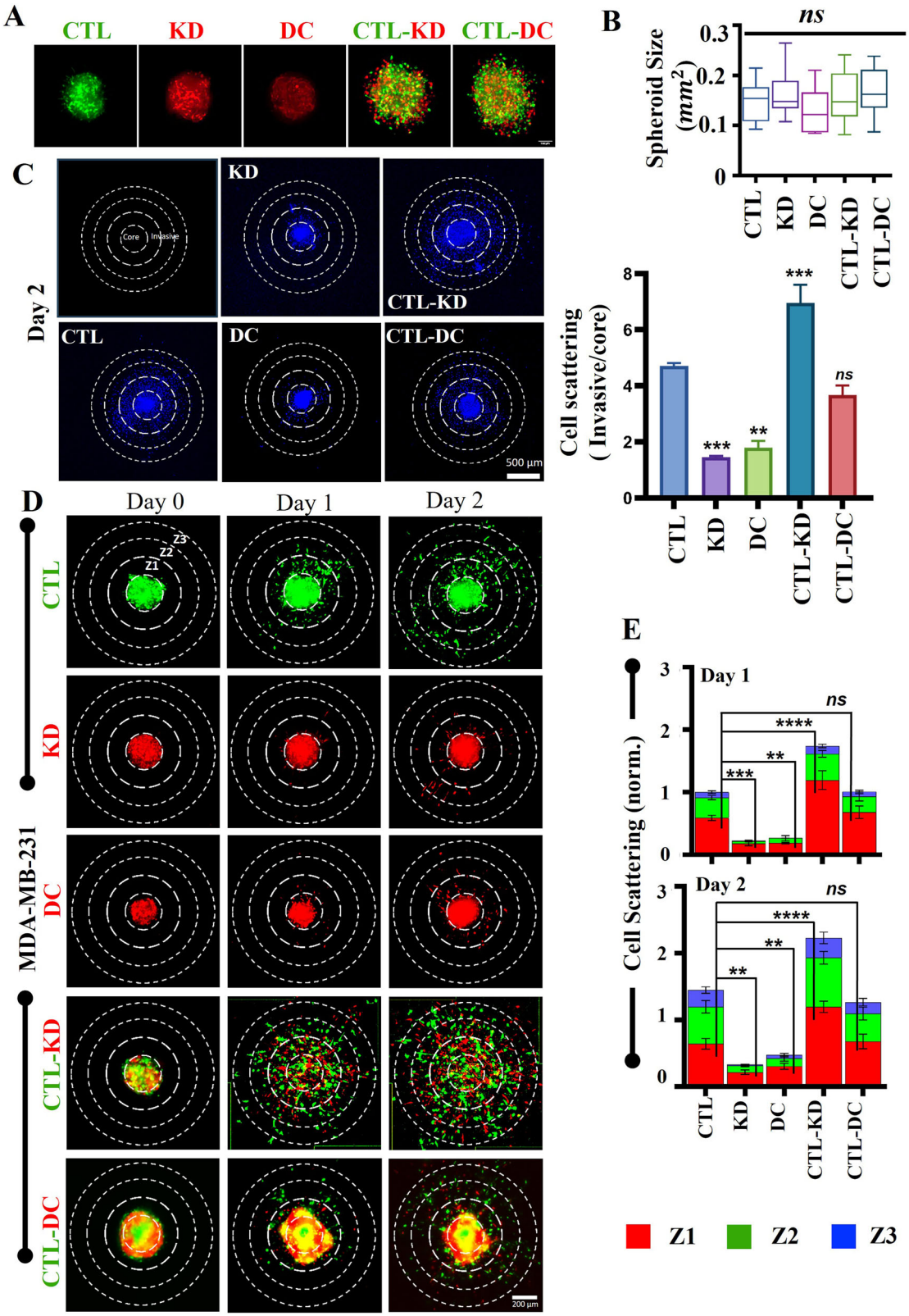

dilution) and APC-conjugated MMP9 antibody (Invitrogen, Cat # MA545511, 1:200 dilution) for one hour at 4 °C in the dark.

To generate MMP9 knockdown MDA-MB-231 cells, we used lentivirus mediated delivery of anti-MMP9 shRNA construct (Sigma Aldrich, TRCN0000051441, sequence CAGTTTCCATTCATCTTCCAA). Briefly, 5×10^4 cells seeded in 96 well plates were transduced with lentiviral particles containing either MMP9-shRNA (Multiplicity of infection (MOI) of 5) or scrambled shRNA in serum free DMEM containing 8 µg/mL of polybrene (Merck, TR-1003-G). After 24 h of transduction, cells were treated with 4 µg/mL of puromycin (HiMedia, Cat # CMS8861) and incubated for 2–4 days to select for successfully transduced cells (hereafter referred to as shMMP9 cells). MMP9 knockdown was verified using qPCR and western

Fig. 6 | 3D invasiveness of homospheroids and heterospheroids. A Representative images of homospheroids and heterospheroids formed using CTL, KD, and DC cells alone, or by combining CTL cells individually with KD and DC cells. **B** Quantification of homospheroid and heterospheroid sizes ($N \geq 4$ independent experiments). Bar denotes statistical significance (* p value < 0.05). One-way ANOVA with Tukey's post-hoc test was used for comparing means. **C** Representative images of Day 2 spheroids stained with Hoechst and quantification of cell scattering in homospheroids and heterospheroids (Mean ± SEM, $N = 3$ independent experiments). Bar denotes statistical significance (** $p < 0.01$, *** $p < 0.001$, ns: non-significant). One-way ANOVA with Tukey's post hoc test was used for comparing means. **D** Representative images of spheroid invasion over a period of 2 days after implantation in 3D collagen gels. Circles were drawn circumscribing the spheroids at Day 0 (designated at Zone 0 or Z_0), and then drawing concentric circles of width 200 µm, designated as zones Z_1, Z_2 and Z_3, respectively. **E** Quantification of zone-wise cell scattering of CTL, KD, DC, CTL-KD, and CTL-DC spheroids at Day 1 and Day 2 (Mean ± SEM, $N \geq 5$ independent experiments). Bar denotes statistical significance for comparison in Z_1 (** $p < 0.01$, *** $p < 0.001$, **** $p < 0.0001$, ns: non-significant). Two-way ANOVA with Tukey's post hoc test was used for comparing means.

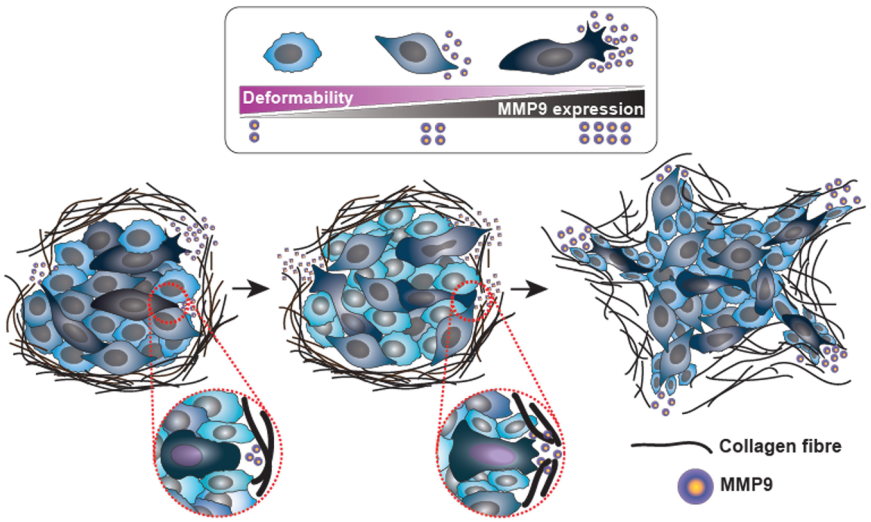

Fig. 7 | Schematic of collective invasion of a proteolytically heterogeneous cell cluster. Differences in biophysical properties enables enrichment of high MMP9 expressing cells at the invasion front and squeezing of softer cells possessing lower MMP9 levels. Collective invasion is driven by high MMP9 expressing cells with low MMP9 expressing cells following behind.

blotting. Scrambled shRNA (Sigma Aldrich, Cat # SHC016) transduced cells were used as shRNA control (shCTL) cells.

For generating fluorescently labeled shCTL and shMMP9 cells, we subcloned eGFP (Addgene plasmid # 13031) and mRFP (Addgene plasmid # 13032) ORF into lentiviral vector pLenti (Addgene plasmid # 39481) using EcoRI and XbaI restriction sites (see Fig. S1 for detailed map of the cloning vector). To generate catalytically inactive MMP9 (MMP9 Δcat), site directed mutagenesis (SDM) was performed by introducing a point mutation of glutamic acid (E) at amino acid position 402 to alanine (A). Briefly, we used the following mutagenesis primer pairs, forward: GCGGCGCATGCGTTCGGCCAC, Reverse: CACGAGGAACAAACTGTATCCTTGGTC, to amplify full MMP9-eGFP-pLenti plasmid (98°C for 3 mins; then 34 cycles of 98 °C for 30 s-68 °C for 30 s-72 °C for 3 min, finally 72 °C for 10 min and put on hold at 4°C) using Phusion High Fidelity Polymerase (Invitrogen, Cat # F530S). Subsequently, the PCR product was used in Kinase-Ligase-DpnI (KLD) reaction using KLD Mixture (NEB, Cat # M0554S) according to the manufacturer's protocol. The clone was verified by DNA sequencing.

Lentiviral particles were produced by transfecting HEK 293T cells with pLenti MMP9Δcat plasmids, lentiviral packaging plasmid psPAX2 (Addgene plasmid # 12260) and viral envelope expressing plasmid pMD2.G (Addgene plasmid # 12259) in 4:3:1 ratio with the help of 25 kDa linear polyethylenimine (PEI, Polysciences, Cat # 23966) solution. The DNA to PEI ratio was 1:3. Cells were incubated for 48 h, followed by harvesting the conditioned media that contains the viral particles. shMMP9 cells expressing MMP9 Δcat plasmid (hereafter referred to as Δcat cells) were transduced as described above, with successfully transduced cells sorted using flow cytometry.

Cell experiments on collagen gels. 3D collagen gels were fabricated by mixing rat tail Collagen type-I solution (Corning Cat. # 354249) with 10x PBS and ice cold DMEM. Next, the pH of the solution was adjusted by adding 1N NaOH solution[22]. Further, the gels were transferred to CO_2 incubator maintained at 37 °C and incubated for 1 h, to complete the gelation process. After 24 h of cell seeding on top of 3D collagen gels (1.2 mg/ml), cells were fixed with 4% paraformaldehyde (PFA) for 15 min. After washing cells thrice with 1x PBS, cells were stained with Wheat Germ Agglutinin (WGA) conjugated with Alexa flour 647 (Invitrogen, Cat # W32466) at 1:500 dilution in PBS overnight. Next day, after washing with 1x PBS, cells were incubated with DAPI (Sigma Aldrich Cat # D9542) at 1:2000 dilution in PBS for 15 min. Fluorescence images were acquired on an inverted microscope (Olympus IX83) at 60x oil immersion objective and the spread area manually quantified using Fiji-ImageJ software. For single cell invasion measurements, after six hours of cell seeding inside 3D collagen gels, live cell three-dimensional (3D) motility was recorded over 12 h at 20-min intervals in a live chamber (TokaiHit) using an IX83 Olympus microscope. Analysis of cell spread area and cell motility was performed using Fiji-ImageJ software. Cell deformability was measured using Atomic Force Microscope (AFM) using pyramidal probes (10 kHz, Asylum Research, Cat # TR400PB). For the measurement of cortical stiffness of the cells, first 500 nm indentation data was fitted with Hertz model as done previously [22,45].

For spheroid invasion experiments, spheroids were generated using the hanging drop method by mixing 10^4 cells with 10 µL DMEM media with 6.25 µg/mL collagen-I solution (Corning, Cat # 354249) and incubation for 48 h at 37 °C in 5% CO_2. For experiments, spheroids were mixed with precursor 3D collagen solution and incubated at 37 °C for gelation and encapsulation of the spheroids. Cell invasion was monitored at day 0 (D0, the day when spheroids were seeded), day 1 (D1) and day 2 (D2) in spinning disk confocal microscope (Yokogawa Electric Corporation, CSU-X1) at 10x magnification and at identical exposure and gain settings. Z-stacks were captured, and the images were analysed in Fiji-ImageJ software. Invasion was quantified by measuring the number of invading cells from the spheroid core.

For assessing cell viability in spheroids at Day 2 (D2), spheroids were stained with Propidium Iodide (PI) (BD Biosciences, Cat # 556463), and imaging was performed using a laser scanning confocal microscope (Carl Zeiss, LSM 780). Subsequently, spheroids were fixed with 4% PFA for 30 min at room temperature. After washing the cells three times with 1x PBS, permeabilization was performed with 0.2% Triton-X for 15 min, followed by blocking with 5% FBS in PBS for 2 h. Next, spheroids were stained with an anti-Ki67 antibody (CST, Cat # 9129) overnight. The following day, after rinsing with PBS three times, cells were incubated with secondary antibody for 3 h (Invitrogen, Cat # A-21244) followed by DAPI (Hoechst 33,342 Merck, Cat # B2261) staining for 30 min at room temperature. Finally, spheroids were imaged using the laser scanning confocal microscope.

Gelatin zymography. For assessing proteolytic activity of shCTL, shMMP9 and Δcat cells, 1×10^6 cells were cultured on 35 mm tissue culture dishes in complete media for 6 h after which media was replaced with serum free DMEM. After 24 h of incubation in serum free DMEM, cell secreted conditioned media (CM) was collected. Equal volume of CM was mixed with 6x non reducing loading buffer (G-Biosciences, Cat # 786-701) and run in 7.5% SDS PAGE copolymerised with 1mg/ml gelatin B (SRL, Cat # 83740). Upon completion of the run, gels were washed with renaturation buffer (2.5% Triton X-100 in water) for 1 h. After this, gels were equilibrated with 1x developing buffer (50 mM Tris-base, 50 mM Tris-HCL, 0.2 mM NaCl, 5 mM $CaCl_2$, distilled H_2O and pH adjusted to 7.8-8) for 1hr at room temperature. Next, gels were incubated for 24 h at 37 °C. Following this, the gels were stained for one hour with staining solution (0.5% Coomassie Brilliant Blue R-250 (SRL, Cat # 93473), followed by de-staining (de-staining solution constitutes 10% methanol, 5% acetic acid in dH_2O), until white degradation spots were visible. The gel images were captured using the Bio-Rad ChemiDoc^{TM} MP Imaging System.

Western blotting. Western blotting of whole cell lysates and CM were performed. To make whole cell lysate, we used RIPA buffer (Sigma Aldrich, Cat # R0278) with 1% protease inhibitor and 1% phosphatase inhibitor. The protein concentrations of the whole cell lysate were determined by Lowry Assay Method[46]. Equal amount of proteins per lane were run under denaturing condition in 10% SDS PAGE. For CM, equal volume was loaded per lane. After the run, proteins were transferred onto 0.22 *mu*m PVDF membranes (Bio-Rad, Cat # 1620177) in ice cold conditions. Next, the blots were blocked using 1% gelatin solution (SRL, Cat # 83740) in 1x TBST (20 mM Tris., 150 mM NaCl., 0.1% Tween 20) for 1hr followed by overnight incubation with anti-MMP9 Recombinant Rabbit Monoclonal Antibody (Invitrogen, Cat # MA5-32705) and anti-GAPDH Rabbit Polyclonal Antibody (Cell Signaling, Cat # 2118). Next, the blots were incubated with anti-rabbit HRP conjugated secondary antibody (Invitrogen, Cat # 31460). All these primary and secondary antibodies were diluted at 1:1000 and 1:10000 respectively in 1x TBST containing 0.1% gelatin. Finally, the blots were developed using ECL-HRP substrate (Advansta, Cat # K-12045-D20) in Bio-Rad ChemiDoc^{TM}MP Imaging System.

Computational methods

In order to study the combined effect of phenotypic and functional heterogeneity on cancer invasion, we adapted our previously published 2-dimensional (2D) Cellular Potts Model (CPM) that has been utilized for studying different biophysical aspects of cancer invasion[9,24,47]. The model consists of a cell cluster initially positioned at the center of a two dimensional ECM lattice (1 mm × 1 mm size) populated with ECM fibers of 2 μm in thickness and 30–40 μm in length, with the remaining empty space corresponding to interstitial fluid. Thus, the simulation lattice comprised of 'cell' pixels, 'matrix' pixels and 'fluid pixels'. The cell cluster of 69 cells comprised of varying proportion of proteolytically active (*p*) and non-proteolytic (*np*) cells, with cell sizes set to the average cell size of shCTL and shMMP9 cells determined experimentally, i.e., $A_p = 856\mu m^2$ and $A_{np} = 400\mu m^2$. Since matrix remodeling is mediated by soluble MMP9 secreted by proteolytically active cells, reaction-diffusion kinetics of MMP9 was incorporated into the CPM model using the equation $\frac{\partial MMP9(\mathbf{x},t)}{\partial t} = D.\nabla^2 MMP9(\mathbf{x},t) - \delta \times MMP9(\mathbf{x},t)$ where $MMP9(\mathbf{x}, t)$ represents the concentration of MMP9 molecules at point $\mathbf{x}$ and time t. D $(1.0 \times 10^{-9}\,cm^2\,sec^{-1})$ and δ $(0.002\,sec^{-1})$ represent the diffusion coefficient and the degradation rate of MMP9, respectively. Since MMP9 activity is dictated by ECM ligand density[19,48], the number of MMP9 molecules secreted by a proteolytically active cell was assumed to be $0.1\,sec^{-1}$ at the site of cell-fiber contact.

Spatiotemporal evolution of the simulation lattice was based on minimization of total energy of the system (E) achieved by randomly choosing a pair of neighboring 'source' and 'target' pixels that do not belong to the same cell, and were either 'cell' or 'fluid' pixels. 'Matrix' pixels were not updated in these Monte Carlo updates. One Monte Carlo step (MCS) corresponds to repeating this exercise M times where M corresponds to the total number of lattice pixels that can be evolved irrespective of whether the moves were accepted or not. An attempt to copy the 'source' pixel to the 'target' pixel was based on Monte Carlo acceptance probability ($\tilde{p}$) depending on the change in the system energy (ΔE) due to the proposed change. While proposed changes were always accepted (i.e., $\tilde{p} = 1$) for $\Delta E \le 0$, for $\Delta E > 0$, $\tilde{p} = e^{-\Delta E/k_B T_m}$ where k_B represents the Boltzmann constant, and T_m represents noise in the system and was set to $0.01T$. The system energy for a given configuration (E) is given by the expression

$$E = \sum_{\forall\, i,j \text{ and } \sigma(i)\neq\sigma(j)} J_{\tau(\sigma(i)),\tau(\sigma(j))} + \sum_{\forall\sigma} \lambda_a (a(\sigma) - a_0)^2 + \sum_{\forall\sigma} \lambda_p (p(\sigma) - p_0)^2 + w(\sigma) \quad (1)$$

where $\sigma(i)$ represents the ID of pixel i and $\tau(\sigma)$ represents the type of cell. The first term in the energy expression (i.e., J_{τ_1,τ_2}) represents the boundary energy per unit length between cells of type τ_1 and τ_2, and represents the adhesion energy between different types of pixels. The adhesion energy between two neighboring cell pixels, i.e., (J_{cc}) was varied to mimic different extents of cell-cell adhesion with $J_{cc} = 1k_BT/L$ mimicking collective cell migration, $J_{cc} = 40k_BT/L$ mimicking single cell migration and $J_{cc} = 16k_BT/L$ representing intermediate level of adhesion indicative of a partial epithelial to mesenchymal (EMT) phenotype. Cell-matrix (J_{cm}), cell-fluid (J_{cf}), matrix-fluid (J_{mf}) and fluid-fluid (J_{ff}) adhesion energies were held constant, i.e., $J_{cm} = 16k_BT/L$, $J_{cf} = 32k_BT/L$, $J_{mf} = J_{ff} = 35k_BT/L$. The second and third terms in the energy equation represent the energy associated with changes in cell size and cell perimeter from their preferred area (a_0) /perimeter (p_0), with the area constraint (λ_a) representing bulk cell stiffness and the perimeter constraint (λ_p) indicative of line tension. The target perimeter (p_0) of a cell of target cell size (a_0) was computed using the formula $2\sqrt{\pi a_0}$. Based on AFM experimental data where shCTL cells were found to be nearly twice as stiff as shMMP9 cells, for most of the simulations, the following values of λ_a and λ_p were assumed for proteolytic ($\lambda_a{}^p, \lambda_p{}^p$) and non-proteolytic ($\lambda_a{}^{np}, \lambda_p{}^{np}$) cells: $\lambda_a{}^p = 1\,E/L^4, \lambda_a{}^{np} = 0.5\,E/L^4, \lambda_p{}^p = 0.5\,E/L^2$ and $\lambda_p{}^{np} = 0.25\,E/L^2$. In simulations where these properties were changed, it is explicitly mentioned. The fourth term of the energy equation corresponds to active motility of the cell due to its inherent polarization and is given by the expression $w(\sigma) = -\mu_0 \hat{\mathbf{p}}$, where μ_0 represents strength of motility and $\hat{\mathbf{p}}$ represents the polarity vector. While μ_0 was assumed to be $50k_BT/L$ for proteolytic cells, and $30k_BT/L$ for non-proteolytic cells, $\hat{\mathbf{p}}$ at a given time was computed by taking the average of previous ten displacement vectors[24].

Simulation implementation, visualization and data analysis. The complete simulation framework was implemented in CompuCell3D (CC3D)[49] with post-processing performed in python to implement custom routines. Detailed description of the simulation implementation is provided in Supplementary text. For visualization, *.vtk files were

generated and visualized in CC3D. Cell translocation was quantified based on cell centroid using custom written scripts in RStudio.

Data availability

CC3D code, PIFF file for the lattice fibers, and the simulation project folder for all combinations of proteolytic and non-proteolytic cells have been deposited in GitHub (https://github.com/shamiks123/MMP9_Heterogeneity).

Received: 2 June 2025; Accepted: 24 September 2025;
Published online: 29 October 2025

References

1. Meacham, C. E. & Morrison, S. J. Tumour heterogeneity and cancer cell plasticity. *Nature* **501**, 328–337 (2013).
2. Tabassum, D. P. & Polyak, K. Tumorigenesis: it takes a village. *Nat. Rev. Cancer* **15**, 473–483 (2015).
3. Chapman, A. et al. Heterogeneous tumor subpopulations cooperate to drive invasion. *Cell Rep.* **8**, 688–695 (2014).
4. Zhou, H., Neelakantan, D. & Ford, H. Clonal cooperativity in heterogenous cancers. *Sem. Cancer Biol.* **64**, 79 – 89 (2017).
5. Swaminathan, V. et al. Mechanical stiffness grades metastatic potential in patient tumor cells and in cancer cell lines. *Can. Res.* **71**, 5075–5080 (2011).
6. Harada, T. et al. Nuclear lamin stiffness is a barrier to 3d migration, but softness can limit survival. *J. Cell Biol.* **204**, 669–682 (2014).
7. Piplani, N., Roy, T., Saxena, N. & Sen, S. Bulky glycocalyx shields cancer cells from invasion-associated stresses. *Trans. Oncol.* **39**, 101822 (2024).
8. Li, Q., Rycaja, K., Chena, X. & Tang, D. G. Cancer stem cells and cell size: A causal link? *Sem. Cancer Biol.* **35**, 191–199 (2015).
9. Asadullah et al. Combined heterogeneity in cell size and deformability promotes cancer invasiveness. *J. Cell Sci*. **134**, jcs250225 (2021).
10. Cheung, K. J. et al. Polyclonal breast cancer metastases arise from collective dissemination of keratin 14-expressing tumor cell clusters. *Proc. Nat. Acad. Sci. (USA)* **113**, E854–63 (2016).
11. Kaushik, S., Pickup, M. W. & Weaver, V. M. From transformation to metastasis: deconstructing the extracellular matrix in breast cancer. *Can. Met. Rev.* **35**, 655–667 (2016).
12. Egeblad, M. & Werb, Z. New functions for the matrix metalloproteinases in cancer progression. *Nat. Rev. Cancer* **2**, 161–174 (2002).
13. Wolf, K. et al. Multi-step pericellular proteolysis controls the transition from individual to collective cancer cell invasion. *Nat. Cell. Biol.* **9**, 893–904 (2007).
14. Bohn, G., Liden, B., Schultz, G., Yang, Q. & Gibson, D. J. Ovine-based collagen matrix dressing: next-generation collagen dressing for wound care. *Adv. wound care* **5**, 1–10 (2016).
15. Mondal, S., Adhikari, N., Banerjee, S., Amin, S. A. & Jha, T. Matrix metalloproteinase-9 (MMP-9) and its inhibitors in cancer: A minireview. *Eur. J. Med Chem.* **194**, 112260 (2020).
16. Choi, Y. A., Kim, D. K., Bang, O. S., Kang, S. S. & Jin, E. J. Secretory phospholipase a2 promotes mmp-9-mediated cell death by degrading type i collagen via the erk pathway at an early stage of chondrogenesis. *Biol. Cell* **102**, 107–119 (2010).
17. Bigg, H. F., Rowan, A. D., Barker, M. D. & Cawston, T. E. Activity of matrix metalloproteinase-9 against native collagen types I and III. *FEBS J.* **274**, 1246–1255 (2007).
18. Levental, K. R. et al. Matrix crosslinking forces tumor progression by enhancing integrin signaling. *Cell* **139**, 891–906 (2009).
19. Das, A., Monteiro, M., Barai, A., Kumar, S. & Sen, S. MMP proteolytic activity regulates cancer invasiveness by modulating integrins. *Sci. Rep.* **7**, 14219 (2017).
20. Dutta, S., Sarkar, S., Tolani, S., Hazari, A. & Sen, S. Two distinct integrin binding sites on mmp9 drive cancer invasion by mediating integrin membrane trafficking & stabilization. *BioRxiv* 2024.04.01.587542 (2024).
21. Kumar, S., Das, A. & Sen, S. MMP secretion rate and inter-invadopodia spacing collectively govern cancer invasiveness. *Biophys. J.* **114**, 650–662 (2018).
22. Das, A., Barai, A., Monteiro, M., Kumar, S. & Sen, S. Nuclear softening is essential for protease-independent migration. *Matrix Biol.* **82**, 4–19 (2019).
23. Saha, S. K., Sarkar, M., Srivastava, M., Dutta, S. & Sen, S. Nuclear α-actinin-4 regulates breast cancer invasiveness and EMT. *Cytoskeleton* **82**, 145–157 (2025).
24. Kumar, S., Kapoor, A., Desai, S., Inamdar, M. M. & Sen, S. Proteolytic and non-proteolytic regulation of collective cell invasion: tuning by ECM density and organization. *Sci. Rep*. **6**, 19905 (2016).
25. Patwardhan, S., Mahadik, P., Shetty, O. & Sen, S. ECM stiffness-tuned exosomes drive breast cancer motility through thrombospondin-1. *Biomaterials* **279**, 121185 (2021).
26. Pastushenko, I. et al. Identification of the tumour transition states occurring during emt. *Nature* **556**, 463–468 (2018).
27. Jolly, M. K., Manib, S. A. & Levine, H. Hybrid epithelial/mesenchymal phenotype(s): The 'fittest' for metastasis? *BBA Rev. Cancer* **1870**, 151 – 157 (2018).
28. Pastushenko, I. & Blanpain, C. Emt transition states during tumor progression and metastasis. *Trends Cell Biol.* **29**, 212–226 (2019).
29. Sahoo, S. et al. Increased prevalence of hybrid epithelial/mesenchymal state and enhanced phenotypic heterogeneity in basal breast cancer. *iScience* **27**, 110116 (2024).
30. Bocci, F. et al. Toward understanding cancer stem cell heterogeneity in the tumor microenvironment. *Proc. Nat. Acad. Sci. (USA)* **116**, 148–157 (2019).
31. Zanotelli, M. et al. Regulation of ATP utilization during metastatic cell migration by collagen architecture. *Mol. Biol. Cell* **29**, 1–9 (2018).
32. Zanotelli, M. et al. Energetic costs regulated by cell mechanics and confinement are predictive of migration path during decision-making. *Nat. Commun.* **10**, 4185 – 4212 (2019).
33. Zanotelli, M. et al. Highly motile cells are metabolically responsive to collagen density. *Proc. Natl. Acad. Sci. (USA)* **119**, e2114672119 (2022).
34. Yu, Y., Jiang, Y., Glandorff, C. & Sun, M. Exploring the mystery of tumor metabolism: Warburg effect and mitochondrial metabolism fighting side by side. *Cell Signal* **120**, 111239 (2024).
35. Schwager, S. C. et al. Link between glucose metabolism and epithelial- to-mesenchymal transition drives triple-negative breast cancer migratory heterogeneity. *iScience* **25**, 105190 (2022).
36. Friedl, P. & Wolf, K. Proteolytic interstitial cell migration: A five-step process. *Can. Met. Rev.* **28**, 129–135 (2009).
37. Haeger, A., Wolf, K., Zegers, M. M. & Friedl, P. Collective cell migration: guidance principles and hierarchies. *Trends Cell Biol.* **25**, 556–566 (2015).
38. Wolf, K. et al. Compensation mechanism in tumor cell migration: mesenchymal–amoeboid transition after blocking of pericellular proteolysis. *J. Cell Biol.* **160**, 267–277 (2003).
39. Graziani, V., Rodriguez-Hernandez, I., Maiques, O. & Sanz-Moreno, V. The amoeboid state as part of the epithelial-to-mesenchymal transition programme. *Trends Cell Biol.* **32**, 228–242 (2022).
40. Te Boekhorst, V. et al. Calpain-2 regulates hypoxia/HIF-induced plasticity toward amoeboid cancer cell migration and metastasis. *Curr. Biol.* **32**, 411–427 (2022).
41. Parlani, M., Jorgez, C. & Friedl, P. Plasticity of cancer invasion and energy metabolism. *Trends Cell. Biol.* **33**, 388–402 (2023).
42. Pally, D., Pramanik, D. & Bhat, R. An interplay between reaction-diffusion and cell-matrix adhesion regulates multiscale invasion in early breast carcinomatosis. *Front. Physiol.* **10**, 790 (2019).

43. Sai Prasanna, C. V., Jolly, M. K. & Bhat, R. Spatial heterogeneity in tumor adhesion qualifies collective cell invasion. *Biophys. J.* **123**, 1635–1647 (2024).
44. Barai, A. et al. Bulky glycocalyx drives cancer invasiveness by modulating substrate-specific adhesion. *PNAS Nexus* **3**, pga335 (2024).
45. Barai, A., Das, A. & Sen, S. Measuring microenvironment-tuned nuclear stiffness of cancer cells with atomic force microscopy. *STAR Protoc.* **2**, 100296 (2021).
46. Lowry, O. H., Rosebrough, N. J., Farr, A. L. & Randall, R. J. Protein measurement with the folin phenol reagent. *J. Biol. Chem.* **193**, 265–275 (1951).
47. Kumar, S., Das, A. & Sen, S. Multicompartment cell-based modeling of confined migration: regulation by cell intrinsic and extrinsic factors. *Mol. Biol. Cell* **29**, 1599–1610 (2018).
48. Das, A., Kapoor, A., Mehta, G. D., Ghosh, S. K. & Sen, S. Extracellular matrix density regulates extracellular proteolysis via modulation of cellular contractility. *J. Carcinog. Mutagen*. **13**, 1–10 (2013).
49. Swat, M. H. et al. Multi-scale modeling of tissues using compucell3d. In *Methods Cell Biol*., vol. **110**, 325–366 (Elsevier, 2012).

Acknowledgements

S.D. was supported by fellowship from the Department of Biotechnology, Govt. of India (Grant No. DBT/2017/IIT-B/850). S.K.S. acknowledges support from the University Grant Commission (UGC), Government of India (BININ04669656 A). We would also like to thank IIT Bombay-IRCC for providing Bio-AFM and confocal microscopy facilities and DST FIST for the FACS facility. SS acknowledges funding support from STARS, Ministry of Education (Grant No. MoE-STARS/STARS-2/2023-0229). S.S. acknowledges consumable support from MP Biomedicals. The authors thank Swetlana Ghosh (PhD student, Department of Biosciences and Bioengineering, IIT Bombay) for helping with confocal microscopy.

Author contributions

Designed research: A., S.D., S.K.S., A.K., S.S. Developed and executed the simulations: A, A.K. Performed the experiments: S.D., S.K.S., N.S., S.V. Analyzed the data: A., S.D., S.K.S., A.K., N.S., S.V. Wrote the manuscript: S.D., S.K.S., A.K., S.S.

Competing interests

The authors declare no competing interests.

Additional information

Supplementary information The online version contains supplementary material available at https://doi.org/10.1038/s41540-025-00601-2.

Correspondence and requests for materials should be addressed to Shamik Sen.